ARTICLE OPEN

Check for updates

Electron–plasmon and electron–magnon scattering in ferromagnets from first principles by combining *GW* and *GT* self-energies

Dmitrii Nabok [ID][1][✉], Stefan Blügel [ID][1][✉] and Christoph Friedrich [ID][1][✉]

This work combines two powerful self-energy techniques: the well-known *GW* method and a self-energy recently developed by us that describes renormalization effects caused by the scattering of electrons with magnons and Stoner excitations. This *GT* self-energy, which is fully **k**-dependent and contains infinitely many spin-flip ladder diagrams, was shown to have a profound impact on the electronic band structure of Fe, Co, and Ni. In the present work, we refine the method by combining *GT* with the *GW* self-energy. The resulting *GWT* spectral functions exhibit strong lifetime effects and emergent dispersion anomalies. They are in an overall better agreement with experimental spectra than those obtained with *GW* or *GT* alone, even showing partial improvements over local-spin-density approximation dynamical mean-field theory. The performed analysis provides a basis for applying the *GWT* technique to a wider class of magnetic materials.

INTRODUCTION

Many-body spin excitations in interacting electron systems are complex quantum mechanical processes that are fundamental for the description of the properties of magnetic materials. In the field of spintronics, the interaction between conduction electrons and collective spin excitations is critical for explaining the temperature dependence of resistivity and magnetotransport[1]. There is experimental evidence that the scattering of propagating electrons and holes on collective and single-particle spin excitations in magnetic materials lead not only to a renormalization of the quasiparticle band dispersion but also to the appearance of characteristic band anomalies in the quasiparticle spectra measured by the angle-resolved photoemission spectroscopy (ARPES)[2–6], a claim that was very recently corroborated by a common theoretical and experimental study of photoemission in iron[7]. Furthermore, spin fluctuations are considered as one of the key mechanisms to mediate the Cooper pairing in high-T_c superconductors such as cuprates and iron-based pnictides[8–10].

The elementary ferromagnets Fe, Co, and Ni are prototypical model systems to study the effects of the electron–magnon interaction. Progress in photoemission spectroscopy made it possible to obtain ARPES spectra in high energy and momentum resolution, sufficient to resolve anomalies that may appear in the quasiparticle band dispersion as indicators of genuine many-body scattering processes, such as magnon-induced renormalization effects. This opens an important source of information for theorists to develop and test new theoretical approaches.

Although Kohn-Sham (KS) spin-density-functional theory (DFT) is a well-established and powerful tool to describe magnetic materials[11], it is limited to groundstate properties in practice, unable to yield accurate excitation energies and lifetime broadenings, which would be relevant for the interpretation of photoemission spectra. Nevertheless, it does provide a reference system on which more advanced first-principles approaches are based. One of these methods is the dynamical mean-field theory

(DMFT), which maps the interacting many-body system onto a minimal Anderson impurity model[12,13] containing only a small number of electrons, making it possible to include correlation effects to high orders. However, DFT+DMFT suffers from several restrictions: the self-energy is strictly local, its **k** dependence is therefore lost. The electron–electron interaction is described by parameters (*U* and *J*), which are often fitted to experiment or treated as free parameters, limiting the predictive power of the method, and there is a double-counting problem related to the treatment of exchange and correlation between DMFT and the DFT reference.

Therefore, we resort to an alternative theoretical framework, the many-body perturbation theory (MBPT), which is not subjected to these restrictions. Practical calculations rely on an approximation to the electronic self-energy $\Sigma(\mathbf{r}, \mathbf{r}'; \omega)$, which describes the many-body exchange and correlation processes that an electron or hole experiences while propagating through a material[14]. The widely used *GW* self-energy approximation[15] is one such approximation. It has been applied to Fe, Co, and Ni[16–18] and yielded results in better agreement with the experimental values for the bandwidths and the effective masses than KS DFT. Importantly, the *GW* self-energy predicts the bands to be broadened due to lifetime effects. The predicted broadening is, however, way too small compared with what is seen in photoemission spectra. Furthermore, the theoretical spectra do not exhibit any band anomalies, of which there is experimental evidence.

In a recent publication[19], we showed that a different approximation, which we called *GT* self-energy, improves on these shortcomings. The *GT* self-energy describes the scattering of electrons with spin waves and single-particle spin-flip excitations and is thus complementary to *GW*, in which the scattering processes do not involve a spin-flip. Collective spin waves and single-particle excitations are described jointly by a magnetic *T* matrix, constructed from solutions of a spin-flip Bethe-Salpeter equation (BSE). Applying the *GT* self-energy to the elementary

[1]Peter Grünberg Institut and Institut for Advanced Simulation, Forschungszentrum Jülich, Jülich 52425, Germany. [✉]email: d.nabok@fz-juelich.de; s.bluegel@fz-juelich.de; c.friedrich@fz-juelich.de

ferromagnets Fe, Co, and Ni yielded spin-, energy-, and momentum-dependent spectral functions that could be directly compared with photoemission spectra. The theoretical spectral functions revealed strongly renormalized quasiparticle bands with profound lifetime broadening and anomalies in the band dispersion. In particular, a waterfall-like structure in a spin-down valence band at a binding energy of ~1.5 eV was predicted in Fe and later measured by ARPES[7].

Despite these successes, the theoretical GT spectra also showed deficiencies. First, the d bandwidth was overestimated compared with the experiment. Second, the lifetime broadening and band anomalies seemed to be overestimated, as well. For example, the 1.5 eV waterfall structure, while appearing at about the right energy and momentum, has an over-pronounced shape when compared to the experiment. Third, we noticed a violation of causality, manifesting itself in an incorrect change of sign in the imaginary part of the self-energy at high (absolute) energies. This sign change is reflected in the spectral function leading to an unphysical loss of lifetime broadening far away from the Fermi energy and to an equally unphysical negative quasiparticle weight. The latter results in a violation of particle-number conservation because the quasiparticle weights partly cancel each other out when integrated.

We attributed these deficiencies to the fact that the GW self-energy was neglected in the calculations at the time for simplicity[19]. We expressed the expectation that the inclusion of GW would remedy these deficiencies. In the present work, as a continuation of the previous study, we present results calculated with the combination of the GT and the GW approximations, which will be referred to as GWT self-energy in the following. We note that, in contrast to GW and GT, the name GWT should not be read as a formula (as a product of G, W, and T). It is simply a name, whereas both GW and GT are, in fact, formulas [product of G and W (T)]. The name GWT is reminiscent of $GW\Gamma$, the common expression for a vertex-corrected self-energy with the vertex function Γ. In fact, GWT can be understood and written as $GW\Gamma$ with a suitably defined vertex function.

We will demonstrate that the aforementioned problems are solved in the combined approach. In particular, it will be shown that the inclusion of GW removes the violation of causality. Furthermore, we will see that GWT tends to flatten many of the features we have seen earlier in GT calculations but, only in a few cases, suppresses them. In the particular case of the 1.5 eV band anomaly, the agreement with the experiment is further improved by GWT, both in terms of location (energy and momentum) and shape. Finally, we will discuss the effect of the self-energy on the magnetic moments, exchange splittings, and d bandwidths of each material and show that the GWT approach is superior to the other two self-energies and to LSDA.

The combination of GW with T-matrix-based self-energies has been the subject of several works in the literature. Romaniello et al.[20] focus on a joint derivation of GW and GT (and its combination) from fundamental equations of MBPT. The derived approximations are then tested on the Hubbard molecule. Contrary to our approach, their formulation is not free of double-counting terms. Although these terms are uniquely defined in principle, they might not fully cancel if GW and GT are implemented with different numerical approximations. In ref. [21], an approach combining GW with the T matrix, similar to ours, was used to calculate a satellite peak at ~−6 eV in the spectral function of Ni. Zhukov et al.[22] employed the same approach for the analysis of lifetime broadening effects in d states of Fe and Ni, in particular discussing the relative importance of spin-flip and non-spin-flip processes. In both of these works, owing to a double-counting of diagrams in the GW and GT series, an explicit double-counting correction was found to be necessary. By contrast, our formulation is double-counting free. Moreover, we

present the **k**-resolved GWT spectral functions and analyze emergent band dispersion anomalies.

The GWT method has been implemented in the SPEX code[18] within the framework of the full-potential linearized augmented-plane-wave method, which provides a highly accurate basis set[23] for all-electron calculations, equally suitable for itinerant s states as for localized d states, making the LAPW basis the optimal basis set for the treatment of transition elements. The GW method employs a mixed product basis[18,24,25], derived from the LAPW basis. The GT method, on the other hand, employs a Wannier basis set for the representation of the T matrix, a quantity that depends on four points in space. This spatial representation allows an efficient truncation of the short-range screened interaction without sacrificing numerical accuracy.

The article is organized as follows. The theory and the relevant computational details are outlined in the Methods section. The results of applying the GW, GT, and GWT self-energies to the electronic structure of bcc Fe, fcc Co, and fcc Ni are presented in the Results section. We analyze the momentum- and energy-dependent quasiparticle spectral functions and discuss the effects of the combined action of the spin-flip and non-spin-flip scattering processes. As part of our analysis, we provide a detailed comparison between the results obtained with different theoretical approaches and the available experimental values for the magnetic moments, exchange splittings, and d bandwidths. The Discussion section concludes the paper with a summary.

RESULTS

Band structure of iron
Figure 1 presents, for iron, the momentum- and energy-resolved spectral function [Eq. (8)] along with P–Γ–N, as obtained from the
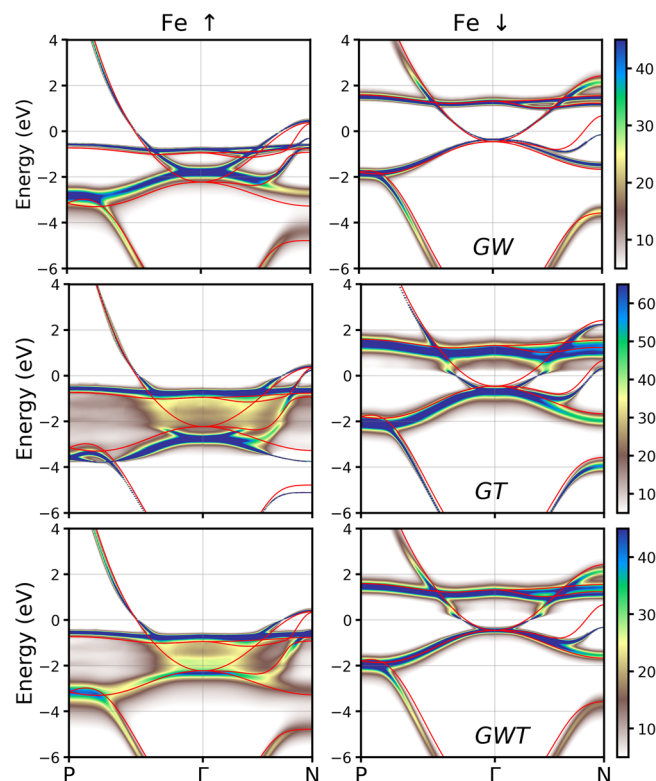
Fig. 1 Renormalized band structures of bcc Fe. Spin majority and minority band structures of bcc Fe renormalized with GW, GT, and GWT self-energies along P–Γ–N. The spectral functions [Eq. (8)] are represented as color-coded 2D plots. The LSDA band structure is shown as red lines.

three self-energies *GW*, *GT*, and *GWT*. For comparison, the LSDA bands are included as red lines. Owing to the explicit electron–electron scattering described by the different self-energies, all renormalized band structures exhibit lifetime broadening of the line widths, however of a rather different magnitude.

As seen in the top panels, the *GW* bands exhibit a well-defined quasiparticle character with the least broadening among the self-energies. The line widths are small close to the Fermi energy and grow towards higher (positive and negative) energies, whereas there is not much difference in lifetime broadening between the two spin channels in contradiction to the experimental observations[3].

The picture changes drastically with the *GT* self-energy. The lifetime broadening still vanishes at the Fermi energy as it must, but, from there, it grows very rapidly, particularly in the majority spin channel, where, in the binding energy range 1–2 eV (negative energies in the plot), the bands disappear completely. Figure 2 shows the renormalized band structure along Γ–N on a smaller energy range and with measured photoemission peak positions. Indeed, between −1 eV and −2 eV there are no experimental points, just where the theoretical spectrum shows the loss of quasiparticle character. This is in marked contrast to the *GW* quasiparticle bands, which remain well-defined throughout this energy range. Similar suppression of quasiparticle character can be seen, albeit to a much lesser degree, in the spin-down channel above the Fermi energy at ~0.5 eV. The lifetime broadening decreases again for larger energies, and the quasiparticle bands reappear. We see a much stronger difference in lifetime broadening between the two spin channels than in *GW*. One can also observe a similar difference between particle and hole (empty and filled) states. Both observations can be explained by the spin selectivity of the electron–magnon scattering[19], which predicts the strongest renormalizations to occur for occupied spin-up and

unoccupied spin-down states. The spin asymmetry of the line broadening is in accordance with experimental measurements[3,7] and also with LSDA+DMFT calculations[26,27].

Combining the two self-energies in *GWT*, we see that the main features of *GT* remain intact. In addition, we observe an important renormalization effect originating from the *GW* self-energy: one of the bands that cross the Fermi energy in LSDA is pushed below the Fermi energy and never crosses it. This effect is seen in both spin channels and for *GW* and *GWT* but not for *GT*. In fact, the consequential missing Fermi surface sheets (forming a hole pocket in the spin-down case) are confirmed in experimental ARPES measurements, where such Fermi surface sheets are not found[28,29]. Moreover, Fig. 2 corroborates this finding, as it does not show any photoemission peaks that would indicate the bands in question to cross the Fermi energy. It does show a photoemission peak position close to the N point that is in favor of the spin-down band to remain below the Fermi energy. This is also consistent with recent quasiparticle self-consistent *GW* calculations[30,31].

It is interesting to note that for the respective spin-up band to show a physically correct band dispersion, it is important to take off-diagonal elements[32] of the *GW* self-energy into account according to Eq. (8) because of strong hybridization effects (that are different in *GW* and LSDA). With the usual *GW* approach of considering only diagonal elements, the bands show unphysical dispersion anomalies, see Fig. 3, where we zoom into the respective energy region along the Γ-N path. The correct dispersion is fully recovered when the 'full' self-energy matrix (diagonal+off-diagonal elements) is taken into account. The reason for this behavior can be understood from comparing the avoided crossings of the (red) LSDA and the (green) *GW* (full) bands close to N. They clearly take place at different momenta. As a consequence, the standard procedure of approximating the quasiparticle wave functions by the KS wave functions [*GW* (diag)] breaks down at that point, and we are forced to calculate the quasiparticle wave function explicitly by diagonalization of the quasiparticle equation [*GW* (full)]. We also see from Fig. 3 that, for the most part, the two *GW* approaches give nearly identical results. This is also true for the spin-down channel of iron as well as for cobalt and nickel. Therefore, we have employed *GW* (full) only for the band structure of iron.

Comparing different self-energies in Fig. 4, it might be surprising at first glance that the combined *GWT* self-energy seems to show less intensity and lifetime broadening than *GT*, whereas one might expect the lifetime effects to increase, rather than decrease, when more diagrams, i.e., more scattering processes, are included. On the one hand, the observation is not completely accurate. For binding energies larger than ~3 eV we clearly see that the lifetime broadening of *GW* dominates, making the *GW* and *GWT* band structures look nearly the same at
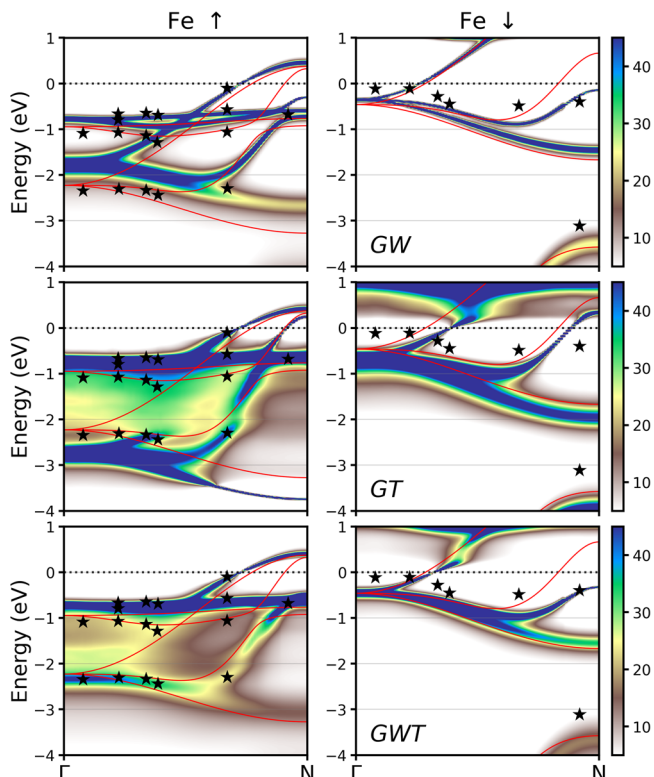
Fig. 2 Comparison of computed and experimental band structures of bcc Fe. Spin-dependent band structures of bcc Fe are renormalized with *GW*, *GT*, and *GWT* self-energies along Γ–N and a smaller energy range. Experimental photoemission peak positions (black stars) are taken from ref. [33].
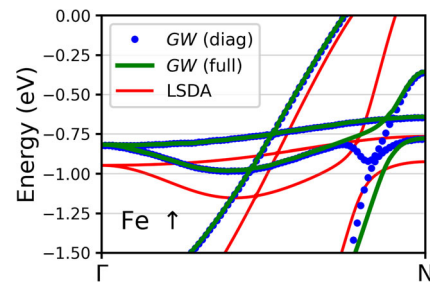
Fig. 3 Role of off-diagonal self-energy matrix elements in bcc Fe. Enlarged view of the iron spin-up band structure obtained from LSDA and two *GW* approaches: one [*GW* (full)] includes off-diagonal elements of the self-energy, the other [*GW* (diag)] does not. For clarity, lifetime broadening is suppressed. *GW* (diag) leads to an unphysical band dispersion close to the N point. Its correction requires the treatment of the self-energy as a full matrix [*GW* (full)].
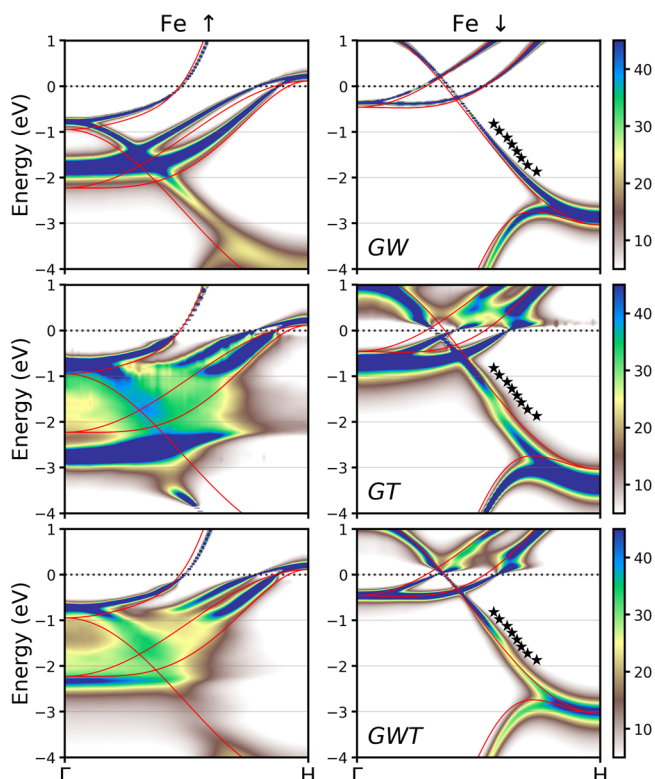
Fig. 4 Renormalized band structures of bcc Fe for Γ–H. Majority and minority band structures of bcc Fe renormalized with *GW*, *GT*, and *GWT* self-energies along Γ–H. Quasiparticle energies extracted from the ARPES spin-down spectrum in the vicinity of the electron–magnon kink[7] are shown by black stars.

larger energies, whereas the *GT* bands become very sharp there. On the other hand, we do see an apparent decrease in the peak broadening at lower binding energies. The bands are narrower again, and certain features become less pronounced, though without disappearing altogether, see, e.g., the spin-down band anomaly just above the Fermi energy. To understand this seeming contradiction, we have to remember that not only do the imaginary parts of the two self-energies add up but also their real parts. The imaginary part gives rise to the line broadening, whereas the self-energy's real part shifts the quasiparticle bands (more generally, the spectral function) energetically. The *GW* self-energy has a rather sizable real part, which, in the present case, shifts the quasiparticle bands away from the energies where the self-energy's imaginary part is large. This detuning effect can ultimately lead to weaker lifetime effects in the *GWT* spectral function.

Comparing the computed band structures with experimental measurements in Fig. 2, one notices that the best agreement is achieved with the *GWT* self-energy. We thus see the strengths of *GW* and *GT* gainfully combined in the *GWT* approach. It is particularly noteworthy that *GWT* yields a flat majority band at a binding energy of 2.34 eV, nicely matching with several photo-emission peak positions at this energy. Interestingly, in LSDA +DMFT[33] this part of the spectrum is completely washed out, offering no explanation for the experimentally measured points.

The inclusion of the electron–magnon scattering does not only lead to pronounced lifetime effects, but it can also give rise to dispersion anomalies in the quasiparticle bands. One such anomaly is a waterfall (kink) structure in the dispersion of a spin-down band of Fe along Γ–H at a binding energy of ~1.5 eV, caused by electron scattering with virtual Stoner excitations. It was recently predicted by us[7,19] and subsequently confirmed

experimentally in high-resolution ARPES[7]. In Fig. 4, the anomaly is shown together with the respective photoemission data. The *GW* renormalization (top panel) moves the band towards the experimental points but does not show any anomaly. The *GT* renormalization alone (middle panel) affects the formation of a kink structure, in agreement with the experiment, albeit at a slightly lower momentum and energy. Furthermore, the shape of the kink appears exaggerated in *GT* compared with the experimental points. If the two renormalizations are combined in the *GWT* method (lower panel), both the shape and location of the dispersion anomaly improve significantly. The band anomaly gets flattened but does not disappear, its shape being in very good agreement with the experimental observation.

Comparing the different renormalized band structures of Fig. 1 reveals a curious and unexpected behavior: although the *GW* and *GT* quasiparticle bands (where they are well-defined) are clearly different from the LSDA band structure (red lines), we find the *GWT* quasiparticle bands surprisingly close to the LSDA bands again. First, we have to emphasize that this is not a general behavior. Even in the same material, a clear difference between *GWT* and LSDA is seen along a different **k** path, Γ–H (Fig. 4). However, the observation hints at a compensating effect that we will encounter again later-on and that deserves to be investigated in more detail.

We do this here by an analysis of the renormalization of the Fe Γ_{25} states at (LSDA) binding energies of 2.19 eV (spin-up) and 0.42 eV (spin-down). Figure 5 presents the *GW*, *GT*, and *GWT* self-energies together with the resulting spectral functions, see the caption for the exact definitions. We also plot the function $\omega - \epsilon_{\mathbf{k}n}^{\sigma}$ (dotted lines). Following the Methods section, the spectral function exhibits the main quasiparticle peak approximately where this linear function intersects with the real part (solid lines) of the respective self-energy. (It is approximate because the imaginary part of the self-energy also has a role regarding the exact peak position—as would the off-diagonal self-energy matrix elements, which are neglected in the present analysis, though.) In the following, we focus on the more interesting spin-up case. At $\epsilon_{\mathbf{k}n}^{\sigma}$ (the node of the linear function), we see that the real parts of the *GW* and *GT* self-energies have approximately the same magnitude but opposite signs. Their sum (green solid line) is thus close to zero and its intersection with the linear function is nearly at the KS energy $\epsilon_{\mathbf{k}n}^{\sigma}$. One also notices that the rate of change of the two real parts is nearly the same but, again, of the opposite sign so that their sum stays in a relatively small window over a quite large energy range (from −2.5 to −0.5 eV). In this range, it exhibits some oscillatory structure, which clearly stems from *GT*, whereas *GW* is rather featureless in the displayed energy range. We can say that while *GW* dominates the overall behavior, it is the *GT* self-energy that provides the fine structure.

Similarly, it is the *GT* contribution that is predominantly responsible for the lifetime effects in the respective energy range. They are nearly an order of magnitude larger than in *GW* and cause an extreme broadening of the quasiparticle states as represented in the corresponding spectral function plot (Fig. 5c–d). However, the imaginary part of *GT* falls off quickly to either side so that it can be seen as a modulation of the smooth parabolic-like behavior of the imaginary part of *GW*. It is the *GW* self-energy that prevails at large binding energies and prevents the imaginary part of *GWT* from becoming negative as happens in the case of the *GT* self-energy below −4 eV. Such a forbidden sign change can be traced back to a violation of the time ordering and, thus, to a violation of causality. We will later come back to this point.

The *GWT* quasiparticle peak is located between the ones from *GT* and *GW*, but its intensity is strongly suppressed. This is because, at the position of the peak, the imaginary part of *GWT* happens to be large, contrary to the cases of *GW* and *GT*. Here, we have an example where the lifetime broadening in *GWT* is not simply the
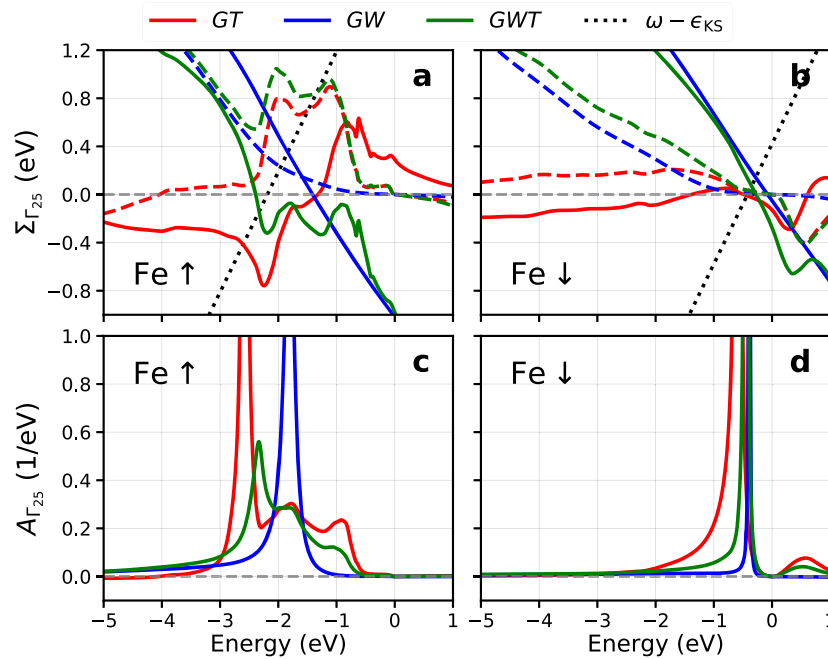
Fig. 5 Self-energies and spectral functions for selected valence states in bcc Fe. The *GW*, *GT*, and *GWT* spin-up and spin-down self-energies (**a**, **b**) and spectral functions (**c**, **d**) for the triple-degenerate Γ_{25} Fe valence states. Solid and dashed lines represent the real and imaginary parts of $\langle\varphi_{\mathbf{k}n}^{\sigma}|\Sigma^{\sigma}(\omega-\Delta_v)-v_{xc}^{\sigma}|\varphi_{\mathbf{k}n}^{\sigma}\rangle$ (*GW* and *GWT*) and $\langle\varphi_{\mathbf{k}n}^{\sigma}|\Sigma^{\sigma}(\omega-\Delta_v)|\varphi_{\mathbf{k}n}^{\sigma}\rangle \mp \Delta_x/2$ (*GT*), respectively. The intersections of the real part with the linear function $\omega-\epsilon_{\mathbf{k}n}^{\sigma}$ are (approximately) the quasiparticle peak positions. The Fermi energy is set at $\omega=0$.

sum of the broadenings from *GW* and *GT*. The *GWT* spectral function, similarly to the *GT* case, shows two side peaks at ~−2 and −1 eV, which bear resemblance to satellite replicas. However, in *GWT* they appear rather as extended shoulders to the main peak than as two distinct peaks as in *GT*. Considering the strong suppression of the *GWT* quasiparticle peak, one might wonder where the quasiparticle weight goes to. The shrinking of the peak is accompanied by a redistribution of weight around the peak, for example, forming the two shoulders. It indeed turns out that the (numerically) integrated areas under the *GW* and *GWT* peaks, despite their different shapes, are very nearly identical. On the other hand, the integral under the *GT* peak is larger (as is obvious to the naked eye) and very close to one. As a consequence, the *GW* and *GWT* peaks integrate to less than one in the presented energy range, namely to ~0.6, which leads to the question: where are the remaining 40%? The question is resolved when one extends the plot to a much larger energy scale: The *GW* (and *GWT*) spectral function displays a very long tail towards larger binding energies where it additionally exhibits a shallow peak (plasmon satellite). If this long tail is fully taken into account, the spectral function, in fact, correctly integrates to one. The long tail can be attributed to the large plasmon energy, present in *GW* and *GWT* but not in *GT*, in which the much smaller magnon energy sets the scale.

The spin-down spectra are less exotic than their spin-up counterparts. The *GT* quasiparticle peak is moderately renormalized to lower energy and has a larger width due to the higher value of the imaginary part of the self-energy with respect to the *GW* peak. The location of the *GWT* peak is close to the one from *GW*. The peak broadening is intermediate between that of *GW* and *GT*, another example that lifetime broadenings do not simply sum, even if the self-energies do.

The renormalized band structures of Fig. 2 look remarkably similar to respective results from LSDA+DMFT[26,27,33]. However, there are differences in the details: (1) we have already commented on the flat majority quasiparticle band at −2.34 eV in *GWT*, which nicely agrees with photoemission peak positions at this energy. LSDA+DMFT, on the other hand, does not show a

distinct feature there, which led the authors of ref. [33] to suspect the peaks to be a surface effect. Similarly, in a plot for Γ − P − H (not shown), we find a flat band at P ~−3.2 eV, which loses intensity quickly towards Γ but persists nearly halfway to the H point. For this **k** range and energy, one indeed observes peaks in ARPES, whereas the LSDA+DMFT ('LDA++') spectrum is basically featureless there[26]. (2) We observe band anomalies caused by electron–magnon scattering, e.g., at ~−1.5 eV in a minority hole band and another at 0.5 eV in a minority electron band. The former is seen in the experiment. We attribute the absence of both effects [(1) and (2)] in DMFT to the spatial restriction imposed by the Anderson impurity. The impurity cannot host extended excited states such as plasmons or spin waves. So, instead of as well-defined many-body states, they rather appear as an incoherent background in the excitation spectrum. (3) LSDA and LSDA+DMFT (and also *GT*) predict extra Fermi surface sheets (a hole pocket in the minority channel) close to the N point, which, according to all available experimental evidence[28,29], do not exist. *GW* and *GWT* pushes the respective bands below the Fermi energy, making the spurious sheets disappear. With all these being said, it should be noticed that *GWT* overestimates the binding energies of the photoemission peak positions in the minority channel. This overestimation is stronger than in LSDA+DMFT. However, one should keep in mind that the present *GWT* approach is free of any adjustable parameters, while the LSDA+DMFT method relies on the *U* parameter, which was chosen in the cited works so as to maximize the agreement of the binding energies with the experiment.

In ref. [19], we presented color plots for the imaginary part of the *GT* self-energy of iron as a function of crystal momentum and frequency. It is the **k** dependence of the self-energy that is one of the fundamental differences between MBPT and DMFT approaches (present in MBPT but missing in DMFT). The addition of the *GW* self-energy into *GWT* gives rise to some important changes and improvements. Figure 6 shows the imaginary part of the *GWT* self-energy expectation value $\Sigma_{\mathbf{k}n}^{\sigma}(\omega-\Delta_v) = \langle\varphi_{\mathbf{k}n}^{\sigma}|\Sigma(\omega-\Delta_v)|\varphi_{\mathbf{k}n}^{\sigma}\rangle$ as a function of **k** and ω for six low-lying bands *n* of Fe and both spins.
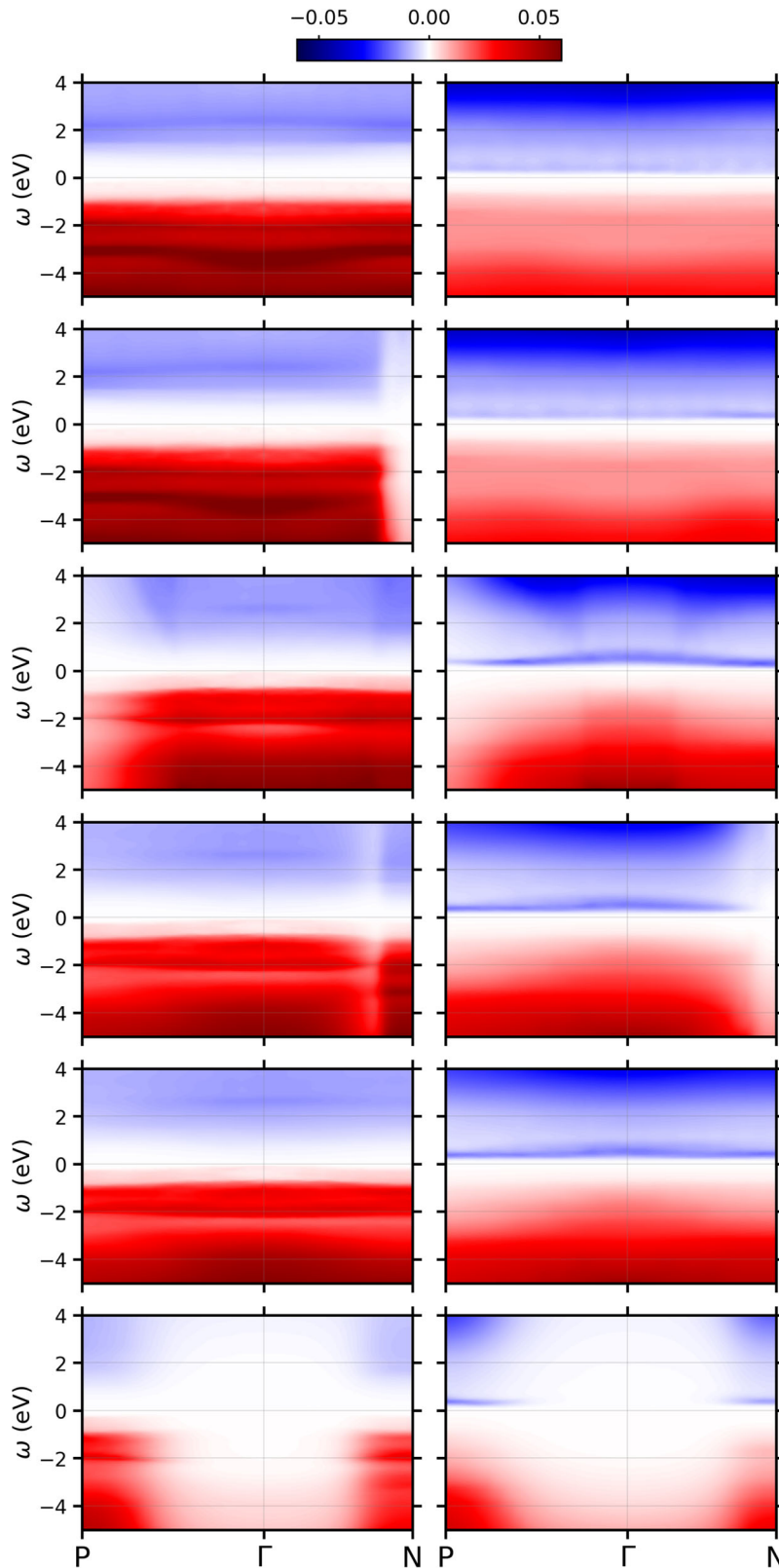
Fig. 6 Momentum and energy dependence of the correlation self-energy in Fe. $\mathrm{Im}\,\Sigma^\sigma_{\mathbf{k}n}(\omega - \Delta_v)$ is shown for the lowest bands and both spins (*cf*. Fig. 1). The bands are ordered with respect to their energy at Γ from bottom to top (same order as in Fig. 10 of ref. [19]).

We use the same plot arrangement as in ref. [19] (Figs. 10 and 11 therein). The plots show a striking similarity to the *GT* plots in a small energy range around the Fermi energy ($\sim -2\,\mathrm{eV} < \omega < 2\,\mathrm{eV}$), again demonstrating that the electron–magnon scattering (*GT*) dominates for small binding energies with intensive peaks below (above) the Fermi energy for the spin-up (spin-down) channel. The main observations made about the plots in ref. [19] hence apply here, too, and we do not want to repeat them.

However, at larger binding energies, *GW* takes over, and here the *GWT* plots clearly deviate from the *GT* ones. One of the most important amendments brought about by including *GW* is seen for larger binding energies in the spin-up channel: the imaginary part of the *GT* self-energy becomes negative at around $\omega = -4$ eV. This is perhaps not so readily seen in Fig. 10 of ref. [19] because the plots show the absolute value of the imaginary part. However, the sign change reveals itself by white lines traversing the diagrams from left to right, marking the regions where the imaginary part vanishes. This change of sign is unphysical. Causality demands the imaginary part of the self-energy to be non-negative (non-positive) for $\omega < 0$ ($\omega > 0$). In ref. [19], we expressed the expectation that the inclusion of *GW* diagrams would restore the correct sign. Indeed, as is evident from Fig. 5, no unphysical sign change is observed at larger binding energies. So, it is the *GW* self-energy that provides the lifetime effects necessary to rectify the picture. (Had we chosen a larger energy scale towards positive ω in Fig. 10 of ref. [19], we would see an analogous effect in the spin-down channel.)

Another noteworthy effect can be observed in the third plot from the top (spin-up and spin-down). These two plots pertain to bands that cross the Fermi surface twice. (The crossings are about halfway between P and Γ as well as close to the N point in the spin-up case, and symmetrically and close to Γ for spin-down.) In the *GWT* plots, one can make out step-like features that go all the way from top to bottom just where the bands cross the Fermi energy. Such features are not found in the corresponding *GT* plots. Closer inspection shows that the step-like feature is not a discontinuous step. It is smoothed out to some extent but remains discernible as a step nonetheless. It turns out that this step has the same mathematical origin as the well-known logarithmic divergence of the group velocity in metallic Hartree-Fock (HF) bands where they cross the Fermi energy. The smoothing of the step has a logarithmic form (with a logarithmic divergence). *GWT* (and *GW*) quasiparticle bands, on the other hand, do not exhibit a logarithmic divergence because there is no divergence right at the Fermi energy ($\omega = 0$). A more-detailed discussion of the logarithmic divergence in *GW* together with its efficient numerical treatment will be presented elsewhere.

Band structure of cobalt and nickel

To complete the series of elementary ferromagnets, we have also carried out *GW*, *GT*, and *GWT* calculations for fcc cobalt and fcc nickel. The corresponding renormalized band structures are compared in Figs. 7 and 8. Cobalt and nickel have fewer empty d states than iron. As a consequence, the phase space of spin excitations is smaller and, hence, we observe a considerably smaller impact of electron–magnon scattering on the electronic structure than in iron. The reduced effect of electron–magnon scattering is particularly evident in nickel, where the *GWT*-renormalized majority and minority band structures look identical to the *GW* ones. They are, of course, not exactly identical, but, by eyesight, it is hard to see any difference. This might be surprising since the *GT* band structures clearly show broadening and energy renormalization. Here, we see an effect that we have already encountered before and that we called a detuning effect: the (comparatively) large real part of the *GW* self-energy shifts the quasiparticle energy into a region where the *GT* self-energy is small and where *GW* dominates. In ref. [19], we discussed weak magnon satellite features in nickel at binding energies of ~0.8 and 1.7 eV. Fig. 8 shows that the *GWT* calculation washes these features out so that they are not visible anymore in the color plot. However, the satellites are still present in the raw data as shoulders to the main quasiparticle peaks (not shown), but certainly too small to be detected in the experiment.

Similar to nickel, there is hardly any difference between the spin-down *GW* and *GWT* band structures of cobalt. Compared
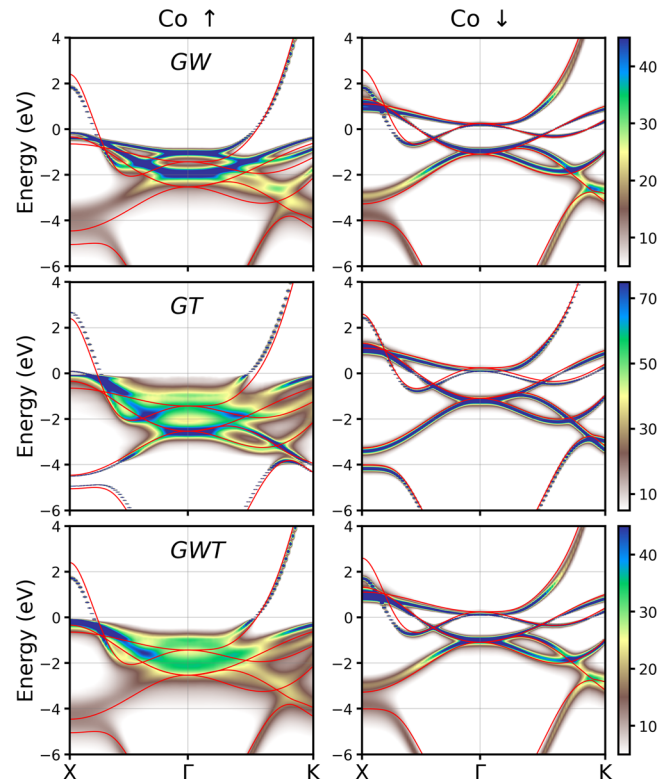
Fig. 7 Renormalized band structures of fcc Co. Spin-dependent band structures of renormalized with *GW*, *GT*, and *GWT* self-energies along X − Γ − K.
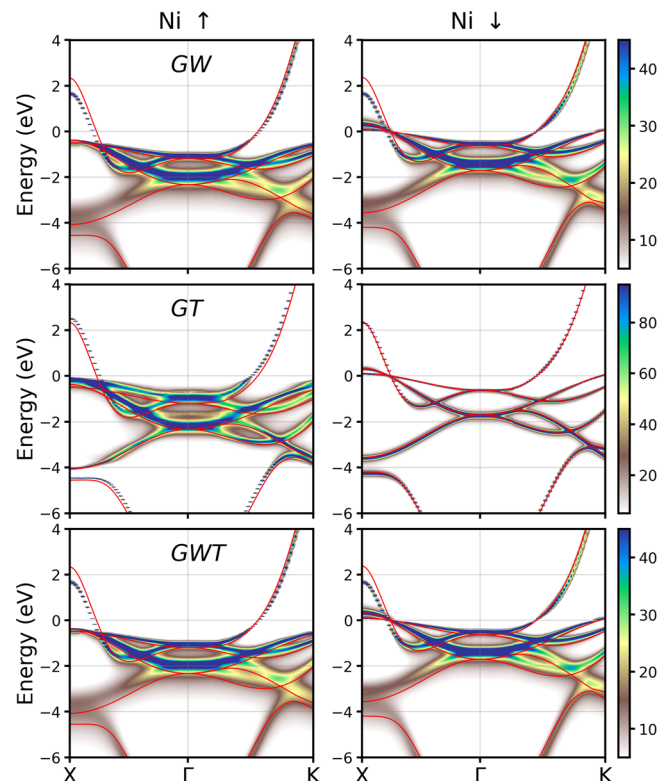
Fig. 8 Renormalized band structures of fcc Ni. Spin-dependent band structures are renormalized with *GW*, *GT*, and *GWT* self-energies along X − Γ − K.

with that, however, we observe a strong lifetime-broadening effect in the spin-up channel from just below the Fermi energy down to binding energy of ~3 eV: the GWT bands are significantly broader than in the case of GW, though not completely losing their quasiparticle character as in iron. The band energies, on the other hand, turn out to be not very different from the GW ones. Furthermore, we see an effect in Co that had gone unnoticed when we collected the results for our previous publication[19]. The GT renormalization produces a tiny spin-up hole pocket at the X point that is neither present in LSDA nor in GW. Renormalizing with the combined GWT self-energy pushes the band in question back below the Fermi energy, and the hole pocket disappears again.

Tables

One of the most important quantities to characterize a spin-polarized system is its magnetic moment. The spin magnetic moment is directly given by an integration over the spin density and is, as such, perfectly computable by spin-density functional theory. In fact, the LSDA magnetic moments of iron, cobalt, and nickel are very close to the experimental results as shown in Table 1, so close that they are hard to match by any theory. (The moments are up to 0.05 μ_B lower than in a previous publication of ours[34]. The small deviations are due to different basis sets used in the two studies. The present study employs a more precise basis for the wave functions.) The table also lists the respective magnetic moments obtained with the GW, GT, and GWT methods. Two kinds of GW results are given. One includes—for consistency with the present GT and GWT calculations—the Δ_x correction (see Methods) for the reference system, and the other does not. The latter value is the one that should be compared to GW values from the literature. We want to emphasize at this point that, as explained in the Methods section, the Δ_x correction is applied to the mean-field reference system but later subtracted in the solution of the Dyson equation. One can say that the two GW values are based on two different starting points, and their difference shows the well-known starting point dependence of GW. We will come back to this point at the end of this section. Neither of the two GW magnetic moments improves on the LSDA values. The ones in the brackets are systematically larger, the others nearly identical to LSDA. The GT moments, on the other hand, quite strongly underestimate the experimental values, far more than LSDA overestimates. Finally, the highest-level theory, the GWT approach, represents a clear improvement over LSDA. We find magnetic moments in very good agreement with the experimental values for iron and cobalt. Nickel is the only exception with a magnetic moment nearly identical to the LSDA value.

When comparing the effect of the different self-energies on the band structures of Fe, Co, and Ni (Figs. 1, 7, and 8), we notice a common behavior: GW shifts the d bands up and contracts them, giving rise to smaller d bandwidths, whereas GT tends to increase the bandwidth. In fact, earlier GW studies[16–18] of the simple ferromagnets reported that the d bandwidths shrink upon renormalization, bringing them closer to experiment for some of

the materials. Since we now seem to have a competing effect by the GT self-energy, it is interesting to investigate the bandwidths obtained with the different self-energies. Table 2 presents a comparison of our values with experimental and theoretical results from the literature. For consistency, we determine the d bandwidth in the same manner as in the experimental studies, namely based on the electron binding energies taken at specific critical points (see footnote 33 of ref. [35]), N_1 for bcc Fe and L_1 for fcc Co, and Ni. The d bandwidths of Fe are given for both spins separately because of the large exchange splitting in this material, whereas the values for Co and Ni are spin-averaged. In agreement with previous studies, we find the GW d bandwidths to be consistently smaller than the LSDA values, thus improving the agreement with the experiment for Co and Ni but leading to underestimated values for Fe. The GT bandwidths, in contrast, tend to be larger than in LSDA. This opposite effect partially compensates for the d-band shrinkage caused by GW in the results obtained from the combined GWT self-energy. In this way, the iron GWT bandwidths now end up very close to the experiment, showing the best agreement among the theoretical methods. In the case of Ni, an early GW study[16] already demonstrated that the d bandwidth decreases by the self-energy renormalization, bringing it in close proximity to the experimental value. As we have seen before, the GT self-energy is marginal in nickel. As a consequence, the bandwidths obtained from GW and GWT are nearly identical. For cobalt, although closer to the experiment than LSDA, there is still a significant over-estimation in both GW and GWT. On the one hand, this might be due to different crystal structures, hcp in experiment vs. fcc in the present study. On the other hand, the corresponding experimental value is given with a large inaccuracy of measurement, and the GWT bandwidth is only just outside the error range. Furthermore, the authors of ref. [36], whereas not giving an explicit value, maintain that the bandwidth is larger than 4 eV, in accordance with all theoretical values.

Table 3 presents the exchange splittings of several valence states at special **k** points, for which experimental measurements are available. LSDA mostly overestimates the experimental exchange splittings, reaching a maximal difference of 0.81 eV in the case of cobalt. GW yields exchange splittings systematically smaller than the ones from LSDA. In particular, with the Δ_x correction in the reference system (values without brackets), GW underestimates nearly all experimental splittings, in some cases quite strongly. We find the opposite trend for the GT exchange splittings. They systematically overestimate the corresponding experimental values. So again, the GWT method is seen to benefit from a compensating effect between GW and GT, and the respective exchange splittings turn out to be close to the

Table 1. Electron spin magnetic moments (in μ_B) of Fe, Co, and Ni computed with different techniques.

	LSDA	GW	GT	GWT	exp[1]
Fe	2.15	2.12 (2.17)	2.00	2.09	2.08
Co	1.58	1.57 (1.65)	1.28	1.54	1.52
Ni	0.58	0.59 (0.65)	0.49	0.59	0.52

GW values in brackets are calculated without the Δ_x correction (see text).
[1]Table 12 of ref. [52].

Table 2. d bandwidths (in eV) for bcc Fe, fcc Co, and fcc Ni obtained from LSDA, GW, GT, and GWT and compared with experimental data.

W_d	LSDA	GW	GT	GWT	exp
Fe $N_{1\uparrow}$	4.74	4.29 (4.30)	5.10	4.67	4.50 ± 0.23[1]
Fe $N_{1\downarrow}$	3.54	3.46 (3.35)	3.96	3.57	3.60 ± 0.20[1]
Co $\langle L_1 \rangle$	4.64	4.18 (4.33)	4.67	4.40	3.8 ± 0.5[2]
					> 4.0[3]
Ni $\langle L_1 \rangle$	4.58	4.12 (4.18)	4.56	4.12	3.9 ± 0.2[4]

The bandwidths are estimated, as in the experiment, based on the specified states. The GW values in brackets are computed without the Δ_x correction (see text).
[1]Ref. [53].
[2]Ref. [37].
[3]Ref. [36].
[4]Ref. [16] (based on experimental data from ref. [2]).

Table 3. The exchange splitting ΔE_x at special **k** points computed with different techniques and compared with available experimental values.

ΔE_x	LSDA	GW	GT	GWT	exp
Fe					
Γ_{25}	1.77	1.41 (1.55)	2.09	1.90	2.08 ± 0.10^1
H_{12}	1.56	1.06 (1.19)	1.64	1.51	1.30 ± 0.30^1
P_4	1.36	0.96 (1.08)	1.50	1.19	1.35 ± 0.10^1
N_2	1.60	1.19 (1.32)	1.78	1.49	1.60 ± 0.15^1
Co					
Γ_{25}	1.44	0.98 (1.24)	1.39	1.18	1.20 ± 0.30^2
Γ_{12}	1.66	1.20 (1.48)	1.49	1.04	0.85 ± 0.20^2
L_3	1.48	1.00 (1.26)	1.33	1.18	1.15 ± 0.40^2
Ni					
L_3	0.56	0.37 (0.51)	0.51	0.37	0.31 ± 0.03^3
X_2	0.52	0.30 (0.45)	0.44	0.31	$\sim 0.2^4$

GW values in brackets are calculated without the Δ_x correction in the reference system (see text).
[1] Ref. [53].
[2] Ref. [37].
[3] Ref. [54].
[4] Ref. [55].

experiment throughout, reaching a maximal deviation of only 0.21 eV for a state in iron. The standard deviations for LSDA, GW, GT, and GWT amount to 0.36, 0.34 (0.33), 0.29, and 0.14 eV, respectively.

The cases of cobalt and nickel deserve a second look. LSDA is known to overestimate the exchange splittings in these materials rather strongly [16,37]. In nickel, the LSDA value is larger by about a factor of two. From the values in the table, we see that the standard GW renormalization (values in brackets) corrects the values in the right direction but only by a small step. Applying GW on the Δ_x-corrected reference system, however, yields exchange splittings close to the experiment. The GWT splittings are nearly identical to the GW ones because the GT self-energy has only a minor role in nickel. This is different in the case of cobalt. While the GW correction is seen to have an effect similar to that of Ni, the exchange splittings change significantly by the GT renormalization. With GW alone, deviations are −0.22, 0.35, and −0.15 eV, and after applying GT (in GWT) they are reduced to merely −0.02, 0.19, and 0.03 eV, respectively.

Finally, we want to have a closer look at the two types of GW values shown in Tables 1–3. Both types rely on one-shot GW approaches but are based on two different reference systems, the standard LSDA mean-field system, which however violates the Goldstone condition [14,38], and the same system where the spin-up and spin-down eigenenergies are shifted with respect to each other with a universal parameter Δ_x (see Methods). In ref. [34], we showed that a self-consistent Coulomb-hole screened-exchange (COHSEX) calculation leads to a change in the exchange splitting that can effectively be mimicked by the parameter Δ_x used in the present work. In this way, besides its original purpose to enforce the Goldstone condition, the parameter can also be interpreted as simulating the missing self-consistency of the one-shot approach. It is important to emphasize that Δ_x is thus introduced and determined to fulfill a physical constraint, and no tuning or fitting between theory and experiment is involved.

The difference between the two GW exchange splittings in Table 3 shows an interesting correlation: for all systems, it amounts approximately to $\Delta_x/2$, which is just half the difference between the underlying two reference systems (Δ_x by definition). To understand this correlation, we write the quasiparticle energy

(see the last paragraph of Methods) in a simplified way as $E^\sigma = \epsilon^\sigma + \Sigma^\sigma(E^\sigma) - v^\sigma_{xc}$, where we have suppressed Δ_v and the band and **k** dependencies. Furthermore, we have only retained the diagonal self-energy matrix elements here (whereas the full self-energy matrix, including off-diagonal elements, has been taken into account in the one-shot GW calculations for the iron band structure). Making another standard approximation by linearizing the self-energy around ϵ^σ eliminates the quasiparticle energy from the right-hand side and gives $E^\sigma = \epsilon^\sigma + Z^\sigma[\Sigma^\sigma(\epsilon^\sigma) - v^\sigma_{xc}]$ with the renormalization factor $Z^\sigma = [1 - d\Sigma^\sigma(\omega)/d\omega|_{\epsilon^\sigma}]^{-1}$. We are interested in the difference of the exchange splitting $\Delta E_x = E^\uparrow - E^\downarrow$ between the two GW calculations

$$\Delta \tilde{E}_x - \Delta E_x = (1 - Z)\Delta_x + Z(\tilde{\Sigma}^\uparrow - \tilde{\Sigma}^\downarrow - \Sigma^\uparrow + \Sigma^\downarrow), \quad (1)$$

where the tilde denotes quantities of the GW calculation based on the Δ_x-corrected reference system. We have used the approximation $Z = \tilde{Z}^\uparrow = \tilde{Z}^\downarrow = Z^\uparrow = Z^\downarrow$ (found to be valid in the present cases) and the fact that $\tilde{v}^\uparrow_{xc} - \tilde{v}^\downarrow_{xc} - v^\uparrow_{xc} + v^\downarrow_{xc} = \Delta_x$ (by definition).

We find the second term of Eq. (1) to be significantly smaller (by a factor of three to six) than the first term, which thus dominates. This, together with the fact that $Z \approx 0.5$ for d states, explains the observed behavior

$$\Delta \tilde{E}_x - \Delta E_x \approx (1 - Z)\Delta_x \approx \frac{\Delta_x}{2}. \quad (2)$$

This leaves us with the question of why the second term of Eq. (1) is small compared with the first, which might appear particularly surprising in light of the fact that the GW approximation contains the HF exchange potential Σ^σ_{HF} (the subscript commonly used for the HF self-energy is 'x', however, we use 'HF' here to avoid confusion with the subscripts in Δ_x and the exchange splitting ΔE_x), and the (one-shot) HF exchange splittings are several times larger than the ones from LSDA, so typically $\Sigma^\uparrow_{HF} - \Sigma^\downarrow_{HF} \gg \Delta E_x^{LSDA}$. Further, the 'difference of differences' $\tilde{\Sigma}^\uparrow_{HF} - \tilde{\Sigma}^\downarrow_{HF} - \Sigma^\uparrow_{HF} + \Sigma^\downarrow_{HF}$ [cf. the right side of Eq. (1)] is typically in the order of Δ_x, reaching a multiple of it for some states, and is thus certainly not smaller than $(1-Z)\Delta_x$ in general. It turns out that the corresponding term in GW is much smaller because of a rather effective cancellation between $\tilde{\Sigma}^\sigma_{HF} - \Sigma^\sigma_{HF}$ and $\tilde{\Sigma}^\sigma_c - \Sigma^\sigma_c$ (separately for $\sigma = \uparrow$ and $\sigma = \downarrow$), where the subscript 'c' refers to the correlation part of the self-energy. The latter can formally be written as $\Sigma_c = iG(W - v)$. Because of metallic screening, we have $W \ll v$, and the dominant term $-iGv$ cancels with the HF self-energy $\Sigma_{HF} = iGv$. This explains the relative smallness of the second term on the right-hand of Eq. (1) with respect to the first term.

DISCUSSION

In summary, we implemented a full frequency- and **k**-dependent (non-Hermitian) non-local self-energy that combines the GW with the GT (T-matrix) diagram. These diagrams describe electron–plasmon and electron–magnon scattering processes, respectively. The GWT self-energy (as we call it) is double-counting free by construction and does not rely on adjustable parameters. It has been implemented in the SPEX code, which is based on the LAPW basis set. As the first application of this method, we studied the electronic properties of the elementary ferromagnets bcc Fe, fcc Co, and fcc Ni and compared with results from LSDA, GW, GT, LSDA+DMFT, and experiment.

In a previous work [19], we had already investigated the effect of the GT self-energy alone and found that it gives rise to strong lifetime broadening close to the Fermi energy and anomalies in the electronic band dispersions such as kinks, waterfall structures, and magnon satellite features. In the present work, we demonstrated that the inclusion of the GW self-energy further improves the description of the electronic structure in several ways: (i) the

lifetime broadening, which appears somewhat exaggerated in *GT*, is less extreme in *GWT*. (ii) we find a good quantitative agreement with photoemission peak positions in iron. (iii) An important improvement concerns a band anomaly at a binding energy of 1.5 eV that we had found in the previous *GT* study and that was subsequently observed in ARPES spectra[7]. We revisited this band anomaly and found it to benefit from the inclusion of *GW* in terms of location in energy and momentum and its shape. (iv) A violation of causality (a wrong sign of spectral function) that had been found in *GT* is healed in the *GWT* self-energy. (v) *GWT* magnetic moments, exchange splittings, and *d* bandwidths are in very good agreement with the experiment, better than those obtained with LSDA or *GW* and *GT* alone. Interestingly, one notices a favorable compensating effect between *GW* and *GT* benefitting the *GWT* method, which is particularly obvious in the tables for the magnetic moments, exchange splittings, and *d* bandwidths (but also noticeable in the spectral functions).

The *GWT* band structures are similar to results from LSDA+DMFT. However, we do find some improvements in the details: (1) *GWT* yields well-defined quasiparticle bands at binding energies of 2.34 eV (at Γ) and 3.2 eV (at P) in good agreement with ARPES peak positions, whereas LSDA+DMFT does not show any distinct feature at the respective energies. (2) Several bands show dispersion anomalies, e.g., the 1.5 eV anomaly in iron mentioned above. (3) In contrast to LSDA+DMFT, *GWT* (also *GW*) corrects wrong LSDA band dispersions in iron, which would falsely predict the existence of Fermi surface sheets (including a spin-down hole pocket) that are not observed in the experiment.

The *GT* self-energy contributes significantly only in the vicinity of the Fermi energy at the energy scale of magnon (and Stoner) excitations. In contrast, the *GW* self-energy becomes dominant beyond that region with a characteristic energy scale of plasmonic excitations. This explains the importance of the combined *GW* + *GT* treatment to cover the entire energy range of electronic excitations. We emphasize that the *GWT* lifetime broadenings (scattering rates) are not simply the sum of the broadenings from *GW* and *GT*. The combination of self-energies that have distinct characteristics in different energy regions can cause a detuning effect: for example, the large real part of the *GW* self-energy can shift (detune) a quasiparticle peak away from an energy region where *GT* would cause a strong lifetime broadening. This can lead to the somewhat counter-intuitive observation that *GWT* may show less (more) lifetime broadening in certain energy regions than any of (the sum of) *GW* and *GT*. Few examples of this effect have been discussed. A more-detailed discussion of the lifetime effects in these materials induced by the combined electron–plasmon and electron–magnon scattering processes is planned for a forthcoming article.

We showed the frequency and **k** dependence of the *GWT* self-energy in the form of a color plot, which, by comparison with an analogous plot[19] for *GT*, demonstrated that no sign problem (violation of causality) appears in *GWT*. Moreover, the color plot revealed a curious step-like behavior of the *GWT* self-energy at a momentum where the corresponding quasiparticle band crosses the Fermi energy. This step is not really a discontinuity in the self-energy but exhibits, in its gradient, a logarithmic divergence, which has the same mathematical origin as the famous logarithmic divergence in the group velocity of metallic HF bands. It is important to note that the corresponding quasiparticle bands themselves are unaffected by this divergence.

The presented method of combining the *GW* and *GT* diagrams are implemented in a one-shot (non-self-consistent) approach, but self-consistency is partially taken into account. To this end, a parameter Δ_v is introduced, which is fixed by a self-consistency condition for the Fermi energy. Another parameter Δ_x needs to be included to enforce the Goldstone condition, which is otherwise violated when using the LSDA Green function in the BSE. This latter parameter can also be interpreted as a second self-consistency condition. Both parameters are thus fixed by exact physical constraints and are therefore no adjustable parameters.

To go beyond this type of self-consistency would require a full iterative scheme. Quasiparticle self-consistent *GW*[31] (complemented by the *GT* self-energy) may spring to one's mind. However, as we have seen, the electron–magnon scattering strongly renormalizes the electronic bands, to the extent that some may completely lose their quasiparticle character. In this case, it is questionable whether the quasiparticle self-consistent *GW* scheme would be applicable, and one might need to employ a fully self-consistent *GWT* approach (in the spirit of fully self-consistent *GW*[39–41]), which would retain all lifetime effects encoded in the imaginary part of the Green function. On the other hand, if we compare our *GWT* results with the self-consistent DMFT results, we find many similarities which suggest that a fully self-consistent *GWT* treatment would not drastically change any conclusions made in our work.

The *GWT* method and its implementation within FLAPW offer new opportunities for re-investigating the electronic structure of magnetic materials with possible applications to antiferromagnets and magnetic insulators. It may also help in elucidating the mechanism of superconductivity in high-T_c materials. The inclusion of spin-orbit coupling into the formalism would make the treatment of more complex non-collinear spin structures possible, which are of importance for spintronic applications. The implementation of further scattering channels, such as described by non-spin-flip electron-hole, electron–electron, and hole–hole ladder diagrams, may prove necessary to describe other complex materials, for example, low-dimensional systems. The *GWT* method is particularly attractive due to its relatively low computational cost. The extra time needed for the *GT* part is similar to a standard *GW* calculation.

METHODS
Theory
The main focus of the present study is the *GWT* self-energy, comprising *GW* and *GT* diagrams

$$\Sigma_\sigma^{GWT} = \Sigma_\sigma^{GW} + \Sigma_\sigma^{GT} \tag{3}$$

(see Fig. 9), and its application to elementary ferromagnets. The theory of the *GT* self-energy and its double-counting-free combination with *GW* was laid out already in a foregoing work. For completeness, we recapitulate the main points in this section. For more details, the reader is referred to ref. [19].
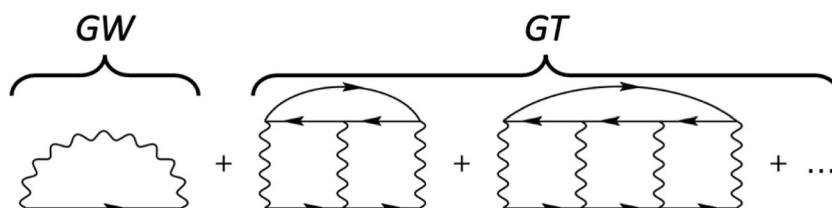
Fig. 9   *GWT* self-energy. Feynman diagrams representing the *GW* (electron–plasmon scattering) and the *GT* self-energy (electron–magnon scattering) are included in the combined *GWT* self-energy.

The self-energy approximations are based on a systematic diagrammatic expansion following the Hedin equations[15]. Although a full self-consistent calculation is not feasible in practice, the Hedin equations can serve as an invaluable tool to derive and improve approximations to the self-energy. The first iteration yields the famous GW approximation[15], commonly used in computational condensed-matter physics[14,42],

$$\Sigma_\sigma^{GW}(1,2) = iG_\sigma(1,2)W(1,2). \tag{4}$$

with the Green function $G_\sigma(1,2)$ for spin-σ particles and the screened interaction $W(1,2)$, calculated within the random-phase approximation. (We use the shorthand $1 = \mathbf{r}_1, t_1$.) However, when applied to the elementary ferromagnets, it becomes obvious that, although GW is an undeniable improvement over KS DFT, it lacks higher-order scattering effects, in particular close to the Fermi energy. We conjectured these scattering processes to be the ones between electrons and magnons, comprising collective spin waves but also renormalized single-particle Stoner excitations, and we argued that these are described by a summation over spin-flip ladder diagrams. We use the term 'magnon' in this general way because the solution of the BSE yields both types of spin excitations at the same time. In general, the resulting many-body excitations are of a mixed collective and single-particle nature. The ladder diagram of lowest order appears in the second iteration of the Hedin equations, each following iteration generating successively higher orders

Summing these diagrams to all orders yields the GT self-energy

$$\Sigma_\sigma^{GT}(1,2) = -i \int d3d4 \, T^{\sigma\sigma'}(13,24)G^{\sigma'}(4,3), \tag{5}$$

where the electron-hole T matrix is determined as a solution of the BSE

$$
\begin{aligned}
T^{\sigma\sigma'}(12,34) = \int d5d6 \, W(12)K^{\sigma\sigma'}(12,56) \\
\times \left\{ W(56)K^{\sigma\sigma'}(56,34)W(34) + T^{\sigma\sigma'}(56,34) \right\}
\end{aligned} \tag{6}
$$

and $\sigma' = -\sigma$. The free electron-hole propagator $K^{\sigma\sigma'}$ is given by

$$K^{\sigma\sigma'}(12,34) = iG^\sigma(13)G^{\sigma'}(42). \tag{7}$$

It is instructive to make a parallel between the GT and the GW self-energies. The T matrix can be viewed as an effective interaction that acts through the exchange of magnons in a similar sense as W incorporates the exchange of plasmons.

It is important to note here that the leading order of the GT self-energy is seen to be the diagram of third order in W. Iterating the Hedin equations does not generate any lower-order direct ladder diagrams. This is because: (1) these are essentially already present in other diagrams, namely in the Hartree 'tadpole' diagram and the GW self-energy. (2) Furthermore, closer inspection shows that they would contain diagrammatic double-counting errors in themselves. This demonstrates the usefulness of the Hedin equations in that the resulting self-energy diagrams are guaranteed to be free of such double-counting errors. In the present case, the double-counting of diagrams is removed by the fact that the GT series starts with the third order in W.

Starting from the third-order GT diagram, however, can give rise to a wrong sign in the imaginary part of the self-energy, which can be interpreted as a violation of causality[19,21]. In ref. [19], we argued that the unphysical sign change occurs in an energy region far away from the Fermi energy, outside the energy range of interest. Therefore, we accepted the wrong sign with the expectation that the inclusion of the GW diagram would restore the correct sign, as we show in Results to be indeed the case.

The present combined GWT self-energy still lacks a number of many-body scattering effects that involve particle–particle (electron–electron, hole–hole, and non-spin-flip electron-hole) scattering as well as high-order exchange processes. These can, in principle, be included with a general T-matrix formulation[20–22], which would, however, go beyond the present paper.

Computational details

MBPT requires as a reference a non-interacting mean-field system. We choose the ground state KS system as that reference system. The self-consistent KS DFT calculations are carried out with the FLEUR code, an all-electron DFT implementation within the FLAPW method. Lattice constants of 2.87 Å, 3.54 Å, and 3.53 Å are employed for Fe, Co, and Ni, respectively. We use the LSDA in the parameterization of Perdew and Zunger[43] for the exchange-correlation functional. The LSDA has been chosen for the reference system to stay consistent with previous works where the same

functional was employed. This choice also facilitates the comparison with the LSDA+DMFT method. For completeness, we have performed GWT calculations for iron with PBE[44] instead of LSDA for the reference mean-field system. The resulting renormalized band structures are very similar to the ones presented here for the LSDA starting point. The LAPW basis set cutoff is 6.2 Bohr^{-1}, and the muffin-tin radius is 2.2 Bohr for all systems. The Brillouin zone (BZ) is sampled with a $14 \times 14 \times 14$ $\mathbf{k}$-point grid.

The quasiparticle band structures are computed perturbatively on top of the LSDA eigensolutions, an approach commonly called 'single-shot' or (specifically for the GW approximation) G_0W_0 calculations. However, a self-consistency condition for the Fermi energy is included, as explained further below. The BZ is sampled with a $10 \times 10 \times 10$ $\mathbf{k}$-grid and 200 empty states are used in summations over unoccupied states (involving KS states up to 15 Ha). To represent the high-energy states accurately, we employ additional basis functions given as high-energy local orbitals in the LAPW formalism[45–47]. Two extra sets of local orbitals are added to each angular momentum channel l from 0 to 3, and one set to $l = 4$, amounting to 41 additional basis functions. As in the previous publication, we employ the contour deformation technique[18,19,48] for evaluating the frequency convolution of the self-energy. Frequency meshes along the imaginary axis are chosen to consist of 34 non-uniformly distributed points in intervals from 0 to $2i$ Ha for GT and from 0 to $10i$ Ha for GW. Integrals along the real axis are computed using uniform frequency grids with increments of 1 mHa and 20 mHa for GT and GW, respectively.

In the T matrix, the screened interaction $W(\omega)$ is approximated by its static limit $W(\omega \to 0)$. This is common practice in BSE calculations and a choice out of necessity: without the static approximation, the BSE would contain three coupled frequencies, which would make the equation untractable for real systems. The static approximation eliminates two of the frequencies, and the equation becomes solvable by matrix inversion. The static approximation is also motivated by the ω dependence of the screened interaction. Besides, the screened interaction $W(\omega)$ is nearly constant in the range of the low-energy magnonic excitations ω, which indicates that for all practical purposes the static approximation is a viable approximation, as is indeed corroborated by our results.

The screened Coulomb interaction W is short-range in metallic systems. This fact has motivated us to employ an on-site approximation for the interaction, i.e., only electrons that occupy the same atomic site are allowed to interact with each other, whereas the interaction of electrons on different sites is neglected. We have tested this approximation[34] and found it to be a very good one for the systems studied in this work. It should be noted that the formalism can be generalized straightforwardly in a way that avoids the on-site approximation, but the notation would become more complex, which is why we restrict ourselves to the on-site treatment in this paper.

The non-self-consistent one-shot self-energy renormalization, as it is carried out in this work, is known to (potentially) violate particle-number conservation in metals[49]. As a simple remedy, one could determine a new Fermi energy according to the renormalized bands. However, this comes with the problem that the condition of vanishing lifetime broadening at $\omega = 0$ [$\text{Im}\Sigma(\omega = 0) = 0$] is fulfilled for the *old* Fermi energy and not for the *new* one. Furthermore, we will see that band anomalies (kinks, satellites, etc.) can occur close to the Fermi energy. By the re-adjustment of the Fermi energy, these features might shift to a wrong energetic position or even end up on the wrong side of the Fermi surface. For these reasons, we employ a correction scheme originally proposed by Hedin[15], which solves the aforementioned problems in an elegant way. One introduces an energy shift Δ_v in $\Sigma(\omega) \to \Sigma(\omega - \Delta_v)$, which is determined such that the Fermi energy remains unchanged by the self-energy renormalization. In principle, this is a non-linear problem, which, in itself, requires a self-consistent solution, since Δ_v affects the Fermi energy (both before and after renormalization), which, in turn, influences the choice of Δ_v. The self-energy, once calculated, can be reused in each step, however. So, this self-consistent cycle can be performed with little computational overhead. One should take into account, though, that the self-energy needs to be evaluated at all $\mathbf{k}$ points and at all states around the Fermi energy for this calculation. The energy shift Δ_v is identical in the two spin-channels. It can be interpreted[19] as a simple constant shift of the exchange-correlation potential ($v_{xc}^\sigma \to v_{xc}^\sigma + \Delta_v$), used for the underlying KS mean-field system. (It might be surprising that Δ_v should have any effect at all, as it seems to simply shift the energy zero. However, one should not forget that quasiparticle energies are defined absolutely and that such a change, therefore, does have an effect. This issue is further discussed in ref. [19]. In this way, v_{xc} is seen to incorporate, to some extent, information about the renormalized system, which can be understood as low-level

Table 4. List of Δ_v and Δ_x parameters used in the calculations.

	Δ_v (eV)			Δ_x (eV)
	GW	GT	GWT	GW/GT/GWT
Fe	0.78	0.17	0.96	−0.23
Co	0.88	0.08	0.92	−0.43
Ni	0.90	0.02	0.89	−0.23

The parameter Δ_v ensures the conservation of the particle number, and Δ_x enforces the Goldstone condition in the magnon excitation spectra (negative sign corresponds to reduced exchange splitting). See text for details.

self-consistency in the self-energy. For completeness, the actual values of Δ_v are listed in Table 4.

We employ another parameter in GT calculations to enforce the correct long-wavelength behavior of the spin-wave dispersion $\omega(k) \xrightarrow{k \to 0} 0$. This Goldstone condition is violated in BSE (or T-matrix) calculations if the Green function is taken from a standard LSDA calculation[34,38]. As shown in ref. [34], the fulfillment of this condition would require a fully self-consistent calculation with the GW self-energy (or, to be more precise, with a self-energy Σ that obeys $\delta\Sigma_{\uparrow\downarrow}/\delta G_{\uparrow\downarrow} = W$). As a pragmatic approach, we suggested a simple correction to the LSDA solution that enforces the Goldstone condition and which we then showed to yield spin-wave dispersions in good agreement with the self-consistent calculation. The correction is done by introducing a parameter Δ_x[19,34] that shifts spin-up and -down states with respect to each other. Δ_x is varied until the spin-wave excitation energy vanishes in the long-wavelength limit[34]. The fact that the Δ_x correction makes the spin-wave dispersions agree well with self-consistent calculations indicates that this correction, too, can be understood as imposing a self-consistency condition, this time not in the Fermi energy (spin independent, absolute energy alignment) but in the exchange splitting (spin-dependent, relative energy alignment). The Δ_x values used in this work are listed in Table 4. We want to emphasize that the two parameters, Δ_x and Δ_v, are obviously not free parameters. They are determined from exact physical constraints.

Most GW studies focus on the real part of the quasiparticle energies and ignore the imaginary part, which is proportional to the lifetime broadening. We will see that in GT and GWT calculations the lifetime broadening is absolutely crucial, so much so that, in some parts of the renormalized band structure, the quasiparticle character is virtually lost and quasiparticle energies cannot be uniquely determined anymore. Therefore, we directly evaluate the momentum- and energy-resolved spectral function

$$A^\sigma(\mathbf{k}, \omega) = \frac{1}{\pi} \text{sgn}(\epsilon_F - \omega)$$
$$\times \text{Im}\left\{\text{Tr}\left[(\omega \pm \tfrac{\Delta_x}{2})I - H_\mathbf{k}^\sigma - \Sigma_\mathbf{k}^\sigma(\omega - \Delta_v) + V_\mathbf{k}^\sigma\right]^{-1}\right\}, \quad (8)$$

which is an important ingredient in the photocurrent of photoemission spectroscopy and can be directly compared with corresponding experimental ARPES spectra.

Mathematically, the spectral function is the imaginary part of the trace (Tr) over the renormalized Green function, here given in terms of an inverse matrix by virtue of the Dyson equation. The prefactor makes the spectral function positive over the whole energy range. The matrix can be represented by any orthonormal basis. We use the basis of KS eigenfunctions $\{\varphi_{\mathbf{k}n}^\sigma\}$, which makes the KS Hamiltonian $H_\mathbf{k}^\sigma$ diagonal with the diagonal elements $\epsilon_{\mathbf{k}n}^\sigma$. Together with $\pm \Delta_x I/2$ (I is the unit matrix), the KS energies are seen to be corrected as discussed above ($\epsilon_{\mathbf{k}n}^\sigma \to \epsilon_{\mathbf{k}n}^\sigma \mp \Delta_x/2$ for $\sigma = \uparrow$ and $\downarrow$). In general, the self-energy matrix $\Sigma_\mathbf{k}^\sigma(\omega)$ with the elements $[\Sigma_\mathbf{k}^\sigma(\omega)]_{nn'} = \langle\varphi_{\mathbf{k}n}^\sigma|\Sigma^\sigma(\omega)|\varphi_{\mathbf{k}n'}^\sigma\rangle$ is not diagonal, and neither is the double-counting correction $V_\mathbf{k}^\sigma$. We treat the GW self-energy matrix as a full matrix taking into account all off-diagonal elements, whereas the GT self-energy is assumed to be diagonal. The neglect of the off-diagonal GT matrix elements is justified by the fact that the GT self-energy is much smaller than the GW self-energy. The term $V_\mathbf{k}^\sigma$ is included to avoid double counting of exchange-correlation effects, described by v_{xc}^σ of KS DFT and by the self-energy. We employ the following

double-counting corrections: (1) $V_\mathbf{k}^\sigma$ is a full matrix with the elements $(V_\mathbf{k}^\sigma)_{nn'} = \langle\varphi_{\mathbf{k}n}^\sigma|v_{xc}^\sigma|\varphi_{\mathbf{k}n'}^\sigma\rangle \mp \Delta_x\delta_{nn'}/2$ ($\mp$ again referring to $\uparrow$ and $\downarrow$) for the GW and GWT methods, (2) $V_\mathbf{k}^\sigma = 0$ for the GT self-energy because the latter describes correlation effects that are not present in v_{xc} (or $v_{xc} \mp \Delta_x/2$), so no double-counting correction is required.

We want to give a few explanatory remarks in the following. One might wonder why one explicitly includes Δ_x in Eq. (8) when it is subtracted later as part of $V_\mathbf{k}^\sigma$. First, this is true for GW and GWT but not for GT, where $V_\mathbf{k}^\sigma = 0$. Second, the explicit inclusion of Δ_x in Eq. (8) is a reminder that, despite the cancellation (in GW and GWT), the results do depend on the parameter because Δ_x affects the Fermi energy, the Green function, the screened interaction W, and the T matrix and, thus, the self-energy. Although the Δ_x parameter is well justified in GT (and also GWT) calculations as a means to enforce the correct long-wavelength behavior of the magnon dispersion, it might appear questionable to apply it also to GW, which does not contain electron–magnon scattering. However, it does make sense also for GW, not only for the sake of consistency with the other methods but also because, as discussed above, it can be regarded as partial self-consistency. As a final remark, it is helpful to consider Eq. (8) for the case of purely diagonal matrices. The expression in the curly brackets has then the form $\sum_n 1/[\omega - \epsilon_{\mathbf{k}n}^\sigma - \langle\varphi_{\mathbf{k}n}^\sigma|\Sigma^\sigma(\omega - \Delta_v) - v_{xc}^\sigma|\varphi_{\mathbf{k}n}^\sigma\rangle]$, here written down for GW (or GWT), in which case Δ_x cancels. (For GT, one would have to replace v_{xc}^σ by $\mp \Delta_x/2$.) This expression becomes large if any of the denominators is small or even zero. Setting the denominator to zero yields the well-known simplified quasiparticle equation $\omega = \epsilon_{\mathbf{k}n}^\sigma + \langle\varphi_{\mathbf{k}n}^\sigma|\Sigma^\sigma(\omega - \Delta_v) - v_{xc}^\sigma|\varphi_{\mathbf{k}n}^\sigma\rangle$, which is commonly employed in GW studies (usually without Δ_v and often in a further approximated, linearized form). The solution of this non-linear equation would yield in ω the complex quasiparticle energy.

The BSE equation [Eq. (6)] is solved on the basis of localized Wannier functions yielding the T matrix in the same basis set. The Wannier set of s, p, and d orbital characters is built from the 21 lowest KS eigenstates (excluding the deep-lying semi-core states) for each spin channel by projection onto suitable muffin-tin orbitals[50]. We used this Wannier representation already for the calculation of spin waves[38,51], in which case, however, the T matrix contains ladder diagrams starting from the first (instead of the third) order in W.

The Wannier functions are employed only as a local basis for the Bloch wave functions, which simplifies and accelerates the solution of the BSE. They are not used for the purpose of constructing a correlated subspace as in DMFT. Neither does our method require Hubbard U parameters. One can therefore expect the method to depend only a little on details of the Wannier construction. In fact, we found an overall small influence of the choice of Wannier functions on the final GT and GWT spectra.

The $\mathbf{k}$ point integration in GT is based on a special tetrahedron method[48], which is required to efficiently compute BZ integrals of strongly varying functions such as the T matrix.

REFERENCES

1. Žutić, I., Fabian, J. & Das Sarma, S. Spintronics: fundamentals and applications. *Rev. Mod. Phys.* **76**, 323–410 (2004).
2. Eberhardt, W. & Plummer, E. W. Angle-resolved photoemission determination of the band structure and multielectron excitations in Ni. *Phys. Rev. B* **21**, 3245–3255 (1980).
3. Schäfer, J. et al. Electronic quasiparticle renormalization on the spin wave energy scale. *Phys. Rev. Lett.* **92**, 097205 (2004).

4. Higashiguchi, M. et al. Energy band and spin-dependent many-body interactions in ferromagnetic Ni(110): a high-resolution angle-resolved photoemission study. *Phys. Rev. B* **72**, 214438 (2005).

5. Hofmann, A. et al. Renormalization of bulk magnetic electron states at high binding energies. *Phys. Rev. Lett.* **102**, 187204 (2009).

6. Sánchez-Barriga, J., Ovsyannikov, R. & Fink, J. Strong spin dependence of correlation effects in Ni due to stoner excitations. *Phys. Rev. Lett.* **121**, 267201 (2018).

7. Młyńczak, E. et al. Kink far below the Fermi level reveals new electron-magnon scattering channel in Fe. *Nat. Commun.* **10**, 1–5 (2019).

8. Scalapino, D. J. Superconductivity and spin fluctuations. *J. Low. Temp. Phys.* **117**, 179–188 (1999).

9. Mazin, I. I. Superconductivity gets an iron boost. *Nature* **464**, 183–186 (2010).

10. Dai, P. Antiferromagnetic order and spin dynamics in iron-based superconductors. *Rev. Mod. Phys.* **87**, 855–896 (2015).

11. Kübler, J. *Theory of Itinerant Electron Magnetism. International Series of Monographs on Physics*. (Oxford University Press, Oxford, New York, 2000).

12. Georges, A. & Kotliar, G. Hubbard model in infinite dimensions. *Phys. Rev. B* **45**, 6479–6483 (1992).

13. Kotliar, G. et al. Electronic structure calculations with dynamical mean-field theory. *Rev. Mod. Phys.* **78**, 865–951 (2006).

14. Martin, R. M., Reining, L. & Ceperley, D. M. *Interacting Electrons: Theory and Computational Approaches*. (Cambridge University Press, Cambridge, 2016).

15. Hedin, L. New method for calculating the one-particle green's function with application to the electron-gas problem. *Phys. Rev.* **139**, 796–823 (1965).

16. Aryasetiawan, F. Self-energy of ferromagnetic nickel in the *GW* approximation. *Phys. Rev. B* **46**, 13051–13064 (1992).

17. Yamasaki, A. & Fujiwara, T. Electronic structure of transition metals Fe, Ni and Cu in the *GW* approximation. *J. Phys. Soc. Jpn.* **72**, 607–610 (2003).

18. Friedrich, C., Blügel, S. & Schindlmayr, A. Efficient implementation of the *GW* approximation within the all-electron FLAPW method. *Phys. Rev. B* **81**, 125102 (2010).

19. Müller, M. C. T. D., Blügel, S. & Friedrich, C. Electron-magnon scattering in elementary ferromagnets from first principles: lifetime broadening and band anomalies. *Phys. Rev. B* **100**, 045130 (2019).

20. Romaniello, P., Bechstedt, F. & Reining, L. Beyond the *GW* approximation: combining correlation channels. *Phys. Rev. B* **85**, 155131 (2012).

21. Springer, M., Aryasetiawan, F. & Karlsson, K. First-principles *T*-matrix theory with application to the 6 eV satellite in Ni. *Phys. Rev. Lett.* **80**, 2389–2392 (1998).

22. Zhukov, V. P., Chulkov, E. V. & Echenique, P. M. Lifetimes of excited electrons In Fe And Ni: first-principles GW and the *T*-matrix theory. *Phys. Rev. Lett.* **93**, 096401 (2004).

23. Singh, D.J., Nordstrom, L. Planewaves, Pseudopotentials, and the LAPW Method, 2nd edn. Springer (2006). https://doi.org/10.1007/978-0-387-29684-5.

24. Kotani, T. & van Schilfgaarde, M. All-electron GW approximation with the mixed basis expansion based on the full-potential LMTO method. *Solid State Commun.* **121**, 461–465 (2002).

25. Betzinger, M., Friedrich, C., Blügel, S. & Görling, A. Local exact exchange potentials within the all-electron FLAPW method and a comparison with pseudopotential results. *Phys. Rev. B* **83**, 045105 (2011).

26. Katsnelson, M. I. & Lichtenstein, A. I. LDA++ approach to the electronic structure of magnets: correlation effects in iron. *J. Phys.: Condens. Matter* **11**, 1037–1048 (1999).

27. Grechnev, A. et al. Theory of bulk and surface quasiparticle spectra for Fe, Co, and Ni. *Phys. Rev. B* **76**, 035107 (2007).

28. Schäfer, J., Hoinkis, M., Rotenberg, E., Blaha, P. & Claessen, R. Fermi surface and electron correlation effects of ferromagnetic iron. *Phys. Rev. B* **72**, 155115 (2005).

29. Młyńczak, E. et al. Spin-polarized quantized electronic structure of Fe(001) with symmetry breaking due to the magnetization direction. *Phys. Rev. B* **103**, 035134 (2021).

30. Sponza, L. et al. Self-energies in itinerant magnets: a focus on Fe and Ni. *Phys. Rev. B* **95**, 041112 (2017).

31. Okumura, H., Sato, K. & Kotani, T. Spin-wave dispersion of 3*d* ferromagnets based on quasiparticle self-consistent *GW* calculations. *Phys. Rev. B* **100**, 054419 (2019).

32. Aguilera, I., Friedrich, C., Bihlmayer, G. & Blügel, S. *GW* study of topological insulators Bi$_2$Se$_3$, Bi$_2$Te$_3$, and Sb$_2$Te$_3$: beyond the perturbative one-shot approach. *Phys. Rev. B* **88**, 045206 (2013).

33. Sánchez-Barriga, J. et al. Effects of spin-dependent quasiparticle renormalization in Fe, Co, and Ni photoemission spectra: an experimental and theoretical study. *Phys. Rev. B* **85**, 205109 (2012).

34. Müller, M. C. T. D., Friedrich, C. & Blügel, S. Acoustic magnons in the long-wavelength limit: Investigating the Goldstone violation in many-body perturbation theory. *Phys. Rev. B* **94**, 064433 (2016).

35. Himpsel, F. J., Heimann, P. & Eastman, D. E. Band structure measurements and multi-electron effects (satellites) for nearly-filled d-band metals: Fe, Co, Ni, Cu, Ru, and Pd (invited). *J. Appl. Phys.* **52**, 1658–1663 (1981).

36. Heimann, P., Marschall, E., Neddermeyer, H., Pessa, M. & Roloff, H. F. Photoemission and electronic structure of cobalt. *Phys. Rev. B* **16**, 2575–2583 (1977).

37. Himpsel, F. J. & Eastman, D. E. Experimental energy-band dispersions and magnetic exchange splitting for cobalt. *Phys. Rev. B* **21**, 3207–3213 (1980).

38. Friedrich, C., Müller, M. C. T. D., Blügel, S.: In: Andreoni, W., Yip, S. (eds.) Many-Body Spin Excitations in Ferromagnets from First Principles, pp. 1–39. Springer, Cham (2019). https://doi.org/10.1007/978-3-319-42913-7_74-3.

39. Caruso, F., Rinke, P., Ren, X., Scheffler, M. & Rubio, A. Unified description of ground and excited states of finite systems: the self-consistent *GW* approach. *Phys. Rev. B* **86**, 081102 (2012).

40. Kutepov, A. L. Electronic structure of Na, K, Si, and LiF from self-consistent solution of Hedin's equations including vertex corrections. *Phys. Rev. B* **94**, 155101 (2016).

41. Grumet, M., Liu, P., Kaltak, M., Klimeš, J. & Kresse, G. Beyond the quasiparticle approximation: fully self-consistent *GW* calculations. *Phys. Rev. B* **98**, 155143 (2018).

42. Golze, D., Dvorak, M., Rinke, P. The GW compendium: a practical guide to theoretical photoemission spectroscopy. *Front. Chem.* **7** https://doi.org/10.3389/fchem.2019.00377 (2019).

43. Perdew, J. P. & Zunger, A. Self-interaction correction to density-functional approximations for many-electron systems. *Phys. Rev. B* **23**, 5048–5079 (1981).

44. Perdew, J. P., Burke, K. & Ernzerhof, M. Generalized gradient approximation made simple. *Phys. Rev. Lett.* **77**, 3865 (1996).

45. Friedrich, C., Schindlmayr, A., Blügel, S. & Kotani, T. Elimination of the linearization error in *GW* calculations based on the linearized augmented-plane-wave method. *Phys. Rev. B* **74**, 045104 (2006).

46. Nabok, D., Gulans, A. & Draxl, C. Accurate all-electron G_0W_0 quasiparticle energies employing the full-potential augmented plane-wave method. *Phys. Rev. B* **94**, 035118 (2016).

47. Michalicek, G., Betzinger, M., Friedrich, C. & Blügel, S. Elimination of the linearization error and improved basis-set convergence within the FLAPW method. *Comput. Phys. Commun.* **184**, 2670–2679 (2013).

48. Friedrich, C. Tetrahedron integration method for strongly varying functions: application to the *GT* self-energy. *Phys. Rev. B* **100**, 075142 (2019).

49. Schindlmayr, A. Violation of particle number conservation in the *GW* approximation. *Phys. Rev. B* **56**, 3528–3531 (1997).

50. Freimuth, F., Mokrousov, Y., Wortmann, D., Heinze, S. & Blügel, S. Maximally localized Wannier functions within the FLAPW formalism. *Phys. Rev. B* **78**, 035120 (2008).

51. Şaşıoğlu, E., Schindlmayr, A., Friedrich, C., Freimuth, F. & Blügel, S. Wannier-function approach to spin excitations in solids. *Phys. Rev. B* **81**, 054434 (2010).

52. Bonnenberg, D., Hempel, K.A., Wijn, H.P.J. Atomic Magnetic Moment, Magnetic Moment Density, G and G' Factor. https://doi.org/10.1007/10311893_25 (Springer, 1986).

53. Turner, A. M., Donoho, A. W. & Erskine, J. L. Experimental bulk electronic properties of ferromagnetic iron. *Phys. Rev. B* **29**, 2986–3000 (1984).

54. Himpsel, F. J., Knapp, J. A. & Eastman, D. E. Experimental energy-band dispersions and exchange splitting for Ni. *Phys. Rev. B* **19**, 2919–2927 (1979).

55. Raue, R., Hopster, H. & Clauberg, R. Spin-polarized photoemission study on the temperature dependence of the exchange splitting of Ni. *Z. Phys. B Con. Mat.* **54**, 121–128 (1984).

ACKNOWLEDGEMENTS

AUTHOR CONTRIBUTIONS

D.N. performed all the calculations. C.F. implemented the method. D.N. and C.F. wrote the manuscript. S.B. supervised the project.

FUNDING

COMPETING INTERESTS
The authors declare no competing interests.

ADDITIONAL INFORMATION
Correspondence and requests for materials should be addressed to Dmitrii Nabok, Stefan Blügel or Christoph Friedrich.

Reprints and permission information is available at http://www.nature.com/reprints

Publisher's note Springer Nature remains neutral with regard to jurisdictional claims in published maps and institutional affiliations.